Optical damage studies of mercury thiogallate nonlinear crystals for use in 1-μm pumped optical parametric oscillators

Valentin Petrov
Georgi Marchev
Aleksey Tyazhev
Marcus Beutler
Vladimir Panyutin
Marina Starikova
Adolfo Esteban-Martin
Valeriy Badikov
Galina Shevyrdyaeva
Dmitrii Badikov
Manuel Reza
Svetlana Sheina
Anna Fintisova

Optical damage studies of mercury thiogallate nonlinear crystals for use in 1-μm pumped optical parametric oscillators

Valentin Petrov
Georgi Marchev
Aleksey Tyazhev
Max-Born-Institute for Nonlinear Optics and
    Ultrafast Spectroscopy
2A Max-Born-Strasse, D-12489 Berlin, Germany
E-mail: petrov@mbi-berlin.de

Marcus Beutler
APE Angewandte Physik und Elektronik GmbH
Haus N, Plauener Strasse, 163-165
D-13053, Berlin, Germany

Vladimir Panyutin
Marina Starikova
Max-Born-Institute for Nonlinear Optics and
    Ultrafast Spectroscopy
2A Max-Born-Strasse, D-12489 Berlin, Germany

Adolfo Esteban-Martin
Max-Born-Institute for Nonlinear Optics and
    Ultrafast Spectroscopy
2A Max-Born-Strasse, D-12489 Berlin, Germany
    and
ICFO-Institut de Ciencies Fotoniques
Mediterranean Technology Park
08860 Castelldefels
Barcelona, Spain

Valeriy Badikov
Galina Shevyrdyaeva
Dmitrii Badikov
Kuban State University
High Technologies Laboratory
149 Stavropolskaya Street
350040 Krasnodar, Russia

Manuel Reza
Max-Born-Institute for Nonlinear Optics and
    Ultrafast Spectroscopy
2A Max-Born-Strasse, D-12489 Berlin, Germany

Svetlana Sheina
Anna Fintisova
Kuban State University
High Technologies Laboratory
149 Stavropolskaya Street
350040 Krasnodar, Russia

Abstract. We investigated optical damage (surface and bulk) in one of the most promising wide bandgap nonoxide nonlinear crystals, $HgGa_2S_4$, that can be used in $\sim$1-μm pumped optical parametric oscillators (OPOs) and synchronously pumped OPOs (SPOPOs) for generation of idler pulses above 4 μm without two-photon absorption losses at the pump wavelength. The optical damage has been characterized at the pump wavelength for different repetition rates using uncoated and antireflection-coated (mainly with a single layer for pump and signal wavelengths) samples. $HgGa_2S_4$ is the most successful nonlinear crystal (both in terms of output energy and average power) for such OPOs, but optical damage inside the OPO has a lower threshold and represents at present the principal limitation for the achievable output. It is related to peak pulse and not to average intensity, and bulk damage in the form of scattering centers occurs before surface damage. Such bulk damage formation is faster at higher repetition rates. Lower repetition rates increase the lifetime of the crystal but do not solve the problem. The safe pump fluence in extracavity measurements is <1 J/cm^2, which corresponds to $\sim$100 MW/cm^2 for the 8-ns pulse duration (both values peak on-axis). In the OPO, however, peak on-axis fluence should not exceed 0.3 J/cm^2 limited by the formation of bulk scattering centers in orange-phase $HgGa_2S_4$. In the nanosecond OPO regime, the damage resistivity of Cd-doped $HgGa_2S_4$ is higher and that of the almost colorless $CdGa_2S_4$ is roughly two times higher, but the latter has no sufficient birefringence for phase-matching. In SPOPOs operating in the $\sim$100 MHz regime, the damage limitations are related both to the peak pulse and the average intensities, but here $HgGa_2S_4$ seems the best nonoxide candidate to obtain first steady-state operation with Yb-based mode-locked laser pump sources. © *2013 Society of Photo-Optical Instrumentation Engineers (SPIE)* [DOI: 10.1117/1.OE.52.11.117102]

1 Introduction

The mid-IR spectral range (3 to 15 μm) represents a very wide gap, where only few gas but no solid-state lasers (SSLs) have been developed. Indeed, the upper limit of practical SSLs, such as Er^{3+} or Cr^{2+}, extends to $\sim$3 μm. Other transitions at longer wavelengths exist, but temperature quenching of the mid-IR fluorescence (Fe^{2+}) or the lack of suitable pump sources represent basic limitations. In most cases, operation at a low temperature and/or using

pulsed pumping (e.g., for Dy^{3+}) is required. Notwithstanding the recent progress in transition-metal mid-IR lasers, the main approach to cover the mid-IR spectral range on the basis of all-SSL technology is still downconversion, employing nonlinear crystals (NLCs). There are oxide crystals that are partially transparent in the mid-IR but not more than 4 to 5 μm. Indeed, the performance of oxide-based crystals is affected by multiphonon absorption starting in the best case from ~4 μm, and thus nonoxide materials have to be used, such as unary, binary, ternary, and quaternary arsenides, phosphides, sulfides, selenides, or tellurides. Some of these inorganic crystals transmit up to 20 to 30 μm before multiphonon absorption occurs as an intrinsic limit. In contrast with the oxides, which can be grown by well-mastered and harmless hydrothermal, flux, or Czochralski methods, the more complex Bridgman-Stockbarger growth technique in sealed (high atmosphere) ampoules, with volatile and chemically reactive starting components, and is the only method used for large size single-domain nonoxide crystals.This certainly hampered their development all the more since special postgrowth treatments are needed to restore stoichiometry and improve their optical quality. As a matter of fact, such materials exhibit more defects and the residual losses (absorption and scatter) are more than one order of magnitude larger than in the best oxide crystals.

The longer the mid-IR transmission limit, the smaller the bandgap of such nonoxide materials, which means that downconversion will require laser pump sources operating at longer wavelengths or, if such do not exist, cascaded schemes based on oxides in the first stage. Efficient frequency conversion is, however, only possible using pulsed laser sources (femtosecond to nanosecond), and most of the chalcogenide mid-IR crystals will suffer two-photon absorption (TPA) at a pump wavelength of ~1 μm (Nd- or Yb-lasers) because of their low bandgap. Of the nonoxide NLCs with sufficiently large bandgap, many exhibit additional limitations related to residual absorption, birefringence, effective nonlinearity, thermal conductivity, or to the growth, availability, and some optomechanical properties. Operation in the nanosecond regime in optical parametric oscillators (OPOs) is free of restrictions originating from the spectral acceptance or higher-order nonlinear effects and has the best potential for achieving high average power and single pulse energy. Notwithstanding the recent rapid development of Tm/Ho nanosecond laser systems at ~2 μm, Nd- and Yb-based systems in the 1-μm spectral range remain the most powerful and scalable pump sources. Such nanosecond OPOs have been demonstrated, however, only with few nonoxide compounds, whose relevant properties are summarized in Table 1. For comparison, the phase-matching angles and the effective nonlinearity are estimated for a chosen idler wavelength of 6.45 μm.

These NLCs include Ag_3AsS_3 (proustite), $AgGaS_2$ (AGS), $HgGa_2S_4$ (HGS), $LiInSe_2$ (LISe), $LiGaS_2$ (LGS), $BaGa_4S_7$ (BGS), $CdSiP_2$ (CSP), and the solid solution $Cd_xHg_{1-x}Ga_2S_4$. Of them, only AGS is commercially available, while HGS and LISe can be obtained from some laboratories. Table 2 summarizes the OPO characteristics. Idler wavelengths >5 μm (the limit of oxides) have been demonstrated only in few cases.[3,6–10,14,17,18,20–28] The longest wavelength of 11.3 μm has been reached with AGS (Ref. 7) and

the highest energy above 5 μm, equal to 3 mJ, with HGS at 6.3 μm.[17] HGS delivered so far the highest overall energy and average power, 6.1 mJ and 0.61 W, respectively, at 4.03 μm.[15]

Although major progress has been achieved with such OPOs starting from 2005, after we introduced LISe, LGS, CSP, BGS, and $Cd_xHg_{1-x}Ga_2S_4$ as new promising mid-IR NLCs, it can be easily seen from Table 2 that the present state-of-the-art is still quite restricted with respect to all essential output characteristics: idler wavelength, energy, repetition rate, and average power. If the reasons shall be summarized in a single statement it could read as follows: insufficient parametric gain to reach a few times above threshold damage-free operation or low slope efficiency, especially away from degeneracy. Crystal length can greatly reduce OPO threshold, but it is limited not only from high optical quality growth considerations (max. 25 mm in Table 2) but also because residual losses in the clear transparency range are rather high in some crystals like CSP or LISe.

The effective nonlinear coefficient is of course of primary importance to reduce the OPO threshold, too. There exist, however, some fundamental relations between the nonlinearity and the index of refraction. Although the nonlinear coefficients d_{il} may vary a lot, the quantity $\delta = d_{il}/(n^2 - 1)^3 = d_{il}/(\chi^{(1)} - 1)^3$ (Miller's delta) remains almost constant (e.g., within one order of magnitude, Miller's empirical rule). Mid-IR NLCs have $n > 2$, and empirical formulae indicate that the index of refraction depends on the material bandgap as $\sim E_g^{-1/4}$;[29] hence, at $n \gg 1$, $d \sim E_g^{-3/2}$ (here d is some average nonlinearity). The index of refraction also enters the expression for the coupling constant in three-photon parametric interaction equations, and it is not the d-tensor that should be compared for different materials but rather some figure of merit, such as FM $\sim d^2/n^3$, which determines the conversion efficiency. Thus, at $n \gg 1$, one obtains FM $\sim n^9 \sim E_g^{-9/4}$.[29] When comparing operation at different wavelengths one should have in mind that besides the weak dependence (dispersion) of the d_{il} tensor components, which can be estimated from Miller's rule on the basis of the refractive index dispersion, there is much stronger dependence through the coupling constant, and the figure of merit can be redefined as FM* $\sim d^2/(n^3\lambda_1\lambda_2\lambda_3)$. Thus, operation at longer (idler) wavelengths away from degeneracy in general, means higher OPO threshold and lower conversion efficiency, which is a fundamental limitation at a fixed pump wavelength.

Although the number of cavity round-trips is smaller, the OPO threshold in terms of pump fluence is lower with shorter pump pulses. This can be seen from Table 2 where pump durations not exceeding 30 ns have been exclusively employed in Nd-laser pumped OPOs, with one exception, the very first Ag_3AsS_3-based OPO in which surface damage occurred within minutes.[1] This can be understood on the basis of higher optical damage intensity limit when the pulses get shorter, although this increase is slower compared to the pulse peak intensity dependence, i.e., the optical damage threshold depends both on pump fluence and on intensity. Another serious limitation with respect to the repetition rate is evident from Table 2. It is related to a lesser extent to thermal effects like lensing or phase-mismatch caused by local heating as a consequence of residual crystal

Table 1 Compilation of important properties of nonlinear crystals for which optical parametric oscillator (OPO) operation with ~1-μm pump has been demonstrated. The effective nonlinear coefficients d_{eff} (column 3) are calculated at the corresponding phase-matching angle θ or φ (column 2); the nonlinear tensor components, d_{il}, used for this calculation were derived from the literature (column 6) applying Miller's rule (column 7). The wavelength λ_F (fundamental) at which the nonlinear coefficients have been estimated by SHG is also included in column 6.

Crystal Point group Plane	θ/φ (deg) (interaction)	d_{eff} [pm/V]	Thermal conductivity (W/mK)	Bandgap E_g (eV)	Miller's δ (pm/V) or d_{il} (pm/V) at λ_F for SHG	+ Miller's correction (pm/V)
AgGaS$_2$ $\bar{4}2m$	40.50 (oo-e) 45.53 (eo-e)	8.86 13.65	1.4//$\boldsymbol{c}$ 1.5$\perp\boldsymbol{c}$	2.70	$\delta_{36} = 0.12$	$d_{36} = 13.65$
HgGa$_2$S$_4$ $\bar{4}$	45.87 (oo-e) 51.21 (eo-e)	15.57 21.18	2.49-2.85//$\boldsymbol{c}$ 2.36-2.31$\perp\boldsymbol{c}$	2.79	$d_{36} = 27.2$ at 1064 nm	$d_{36} = 24.56$
Cd$_x$Hg$_{1-x}$Ga$_2$S$_4$ ($x = 0.55$) 4	90.00 (oo-e)	24.94	1.8-1.92//$\boldsymbol{c}$ 1.62-1.81$\perp\boldsymbol{c}$ ($x = 0.27 - 0.3$)	3.22 ($x = 0.55$)	$d_{36} = 27.2$ at 1064 nm	$d_{36} = 24.94$
LiGaS$_2$ xz mm2 xy	47.77 (oo-e) 40.36 (eo-e)	4.23 5.50	NA	3.76	$d_{31} = 5.8$ $d_{24} = 5.1$ at 2300 nm	$d_{31} = 5.71$ $d_{24} = 5.21$
LiInSe$_2$ xz mm2 xy	36.97 (oo-e) 41.62 (eo-e)	7.26 10.57	4.7-4.5// $\boldsymbol{x}$ 4.7-4.8// $\boldsymbol{y}$ 5.5-5.8// $\boldsymbol{z}$	2.86	$d_{31} = 11.78$ $d_{24} = 8.17$ at 2300 nm	$d_{31} = 12.08$ $d_{24} = 8.65$
BaGa$_4$S$_7$ xz mm2	12.87 (oo-e)	4.94	NA	3.54	$d_{31} = 5.1$ at 2260 nm	$d_{31} = 5.07$
CdSiP$_2$ $\bar{4}2\,m$	80.46 (oo-e)	90.99	13.6	2.2-2.45	$d_{36} = 84.5$ at 4.56 μm	$d_{36} = 92.27$
Ag$_3$AsS$_3$ $3m$	22.04 (oo-e) 24.01 (eo-e) 65.63 (oe-e)	22.89 16.44 3.35	0.113// $\boldsymbol{c}$ 0.092 $\perp$ $\boldsymbol{c}$	2.2	$d_{31} = 10.4$ $d_{22} = 16.6$ at 10.6 μm	$d_{31} = 12.34$ $d_{22} = 19.70$

absorption rather than to a cumulative damage at higher repetition rates. Thus, most such OPOs were operated at 10 Hz, in rare cases at 100 Hz, and damage-free operation at kilohertz repetition rates has only been achieved with pump pulse durations of 1 ns or less.[24,25,27]

The above makes it clear how detrimental damage effects in mid-IR NLCs are when such crystals are employed in nanosecond OPOs. However, there exists another approach for achieving high efficiency in downconversion to the mid-IR. This is the use of ultrashort pulse sources operating at high (~100 MHz) repetition rates to pump a NLC in a cavity whose round-trip time is matched to this repetition rate. In the steady-state regime, such synchronously pumped OPOs (SPOPOs) can provide high average powers in the mid-IR, while in the burst or macropulse mode, high macropulse energies are possible, too. Although temporal walk-off effects (group-velocity mismatch or spectral acceptance) start playing a role with ultrashort and in particular with femtosecond pulses, thanks to the cavity feedback the peak pump intensity levels, at least in picosecond mid-IR SPOPOs, are comparable to nanosecond OPO devices and higher-order nonlinear effects can be normally ignored. In fact, so far SPOPOs, based on nonoxide NLCs pumped near 1 μm in a single pass, have been operated only in the burst mode (Table 3), basically due to optical damage limitations and thermal issues. This was realized by modulation of the mode-locked pump laser pulse train,[30] simultaneous Q-switching,[31] pulsed pumping of the pump

laser,[32,34,35] or picking a limited sequence of pulses for further amplification.[33] The beam cross-sections and the macropulse durations in such pulsed SPOPOs are also similar to nanosecond OPOs and hence the optical damage problems encountered should be similar. However, additional complications are expected for mid-IR SPOPOs operating in the steady-state regime. On one hand, due to the tight focusing, these are angular acceptance and spatial walk-off effects limiting the interaction length; on the other side, these are thermal effects like phase-mismatch or lensing associated with the high average intensities. The optical damage issues in this case are to some extent related to the average intensity and, in this sense, can be compared to measurements with true continuous-wave (cw) sources. In the femtosecond regime, additional restrictions related to spectral acceptance or higher-order nonlinear effects are expected.

In fact, damage limitations are the main reason why such OPO and SPOPO devices pumped near 1 μm never became commercially available. In Secs. 3 to 5, we summarize our recent observations on optical damage (surface and bulk) effects in HGS, which has been used in 1064-nm pumped OPOs for generation of idler pulses beyond 4 μm. HGS is selected as the crystal with one of the highest FM that delivered the highest OPO output so far. It is the only NLC of the defect chalcopyrite family that has been successfully grown in large sizes to be employed for frequency conversion; however, doping of HGS with Cd (Cd$_x$Hg$_{1-x}$Ga$_2$S$_4$) can be used to improve some of its properties, including damage

Table 2 Nanosecond OPOs based on nonoxide crystals pumped by Nd-lasers.

Crystal type, cut angle	Length (mm)	Pump parameters: λ_P, T_P, rep. rate, mode	Idler tuning range (μm)	Idler energy	Reference
Ag_3AsS_3-I, 30 deg	3.8	1064 nm, 200 ns, 2 kHz, SP, TEM_{00}	ND, DR	NA	1
Ag_3AsS_3-I, 29.5 deg see Ref. 3	10	1065 nm, 26 ns, 2 Hz, SP, TEM_{00}, SF	2.13 to 2.56, DR	>10 μJ	2
Ag_3AsS_3-I, 28 deg	10	1065 nm, 25 ns, 2 Hz, SP, TEM_{00}	2.13 to 8.5, SR	<2.5 μJ at 4.5 μm	3
AGS-I, 50.5 deg	20	1064 nm, 20 ns, 10 Hz, SP, TEM_{00}	2.128 to 4, SR	250 μJ at 2.128 μm	4
AGS-I, 49 deg	20	1064 nm, 10.9 ns, 10 Hz, DP	2.77 to 4.2, SR	120 μJ at 3.5 μm	5
AGS-II, 39.9 deg	25	1064 nm, 10 ns, 3.3 Hz, DP	6.7 to 9.8, SR	1200 μJ at 8.2 μm	6
AGS-II, 45.1 deg	20	1064 nm, 20 to 30 ns, 10 Hz, DP, TEM_{00}	3.9 to 11.3, SR	372 μJ at 6 μm	7
AGS-I, 47 deg	20	1064 nm, 10 to 30 ns, <10 Hz, DP, TEM_{00}	2.6 to 5.3, SR	620 μJ at 4 μm	8–10
HGS-II, 67.5 deg	8	1064 nm, 10 Hz, DP	~3.7 to 4.5, SR	NA	11
HGS-II, 67.5 deg	8	1064 nm, 5 ns, 30 Hz, DP	4.18 to 4.438, SR, TT	3.67 mJ at 4.18 μm	12
HGS-I, 52 deg	6	1064 nm, 30 ns, 10 Hz, SP, TEM_{00}	2.3 to 4.4, SR	360 μJ at 2.37 μm	13
HGS-I, 52.7 deg	10.1	1064 nm, 4.4 ns, 20 Hz, SP	3.69 to 5.69, SR	3.3 mJ at 4.03 μm	14
HGS-I, 52.7 deg	13.4	1064 nm, 8 ns, 100 Hz, DP	<3 to 8, SR	6.1 mJ at 4.03 μm	15
HGS-I, 52 deg	6	1064 nm, 15 ns, 10 Hz, DP, TEM_{00}	3.75 to 4.65, SR, TT	~65 μJ at 4.35 μm	16
HGS-II, 50.2 deg	10.76	1064 nm, 8 ns, 10 Hz, DP	4.5 to 9, SR	3 mJ at 6.3 μm	17
$Cd_xHg_{1-x}Ga_2S_4$−I, $x = 0.21$ to 0.56, 74 to 90 deg	10.9 to 11.6	1064 nm, 22 to 30 ns, 10 Hz, SP, TEM_{00}	2.85 to 8.9, SR, in part NCPM	400 μJ at 3.03 μm 270 μJ at 5.76 μm 110 μJ at 8.9 μm	18
LISe-II, 72 deg	17	1064 nm, 10 ns, 10 Hz, DP	3.34 to 3.82, SR	92 μJ at 3.457 μm	19
LISe-II, 41.6 deg LISe-II, 34 deg	17.6, 24.5	1064 nm, 14 ns, 100 Hz, DP	4.65 to 7.5, SR 5.45 to 8.7, SR	282 μJ at 6.5 μm 116 μJ at 8.4 μm	20–22
CSP-I, 90 deg	8	1064 nm, 14 ns, 10 to 20 Hz, DP	6.2, SR, NCPM	470 μJ at 6.2 μm	23
CSP-I, 90 deg	9.5	1064 nm, 1 ns, 1 kHz, DP	6.117 to 6.554, SR, NCPM, TT	24 μJ at 6.125 μm	24
CSP-I, 90 deg	7	1064 nm, 0.4 ns, 1 to 10 kHz, DP, TEM_{00}, SF	6.15, SR	4.3 μJ at 6.15 μm	25
CSP-I, 90 deg	9.5	1064 nm, 14 ns, 100 Hz, SP	6.125, RISTRA	64 μJ at 6.125 μm	26
LGS-II, 40.6 deg	8	1064 nm, 8 ns, 100 Hz, DP	5.46, SR	134 μJ at 5.46 μm	27
LGS-II, 40.6 deg	8.2	1064 nm, 1 ns, 1 kHz, DP	4.046 to 6.014, SR	1.1 μJ at 5.46 μm	27
BGS-I, 9.2 deg	14.05	1064 nm, 8 ns, 100 Hz, DP	5.5 to 7.3, SR	500 μJ at 6.217 μm	28

Note: SR, singly resonant; DR, doubly resonant; ND, near degeneracy; SF, single frequency; SP, single pump pass; DP, double pump pass; TT, temperature tuning; NCPM, noncritical phase-matching; RISTRA, rotated image singly resonant twisted rectangle; NA, not available.

Table 3 Singly resonant nonoxide synchronously pumped OPOs (SPOPOs) pumped by Nd-lasers.

Crystal type, cut angle	Length (mm)	Pump parameters: λ_P, T_P, T_T, rep. rate micro/macropulses	Idler tuning range (μm)	Idler energy micro/macropulses, idler average power	Reference
AGS-II, 48 deg	2×10	1064 nm, 100 ps, 781 ns, 76 MHz/40 Hz	5.505	79 pJ/4.7 nJ, 6 mW at 5.505 μm	30
AGS-I, 48 deg	30	1064 nm, 145 ps, 260 ns, 76 MHz/2 kHz	3.5 to 4.5	15.7 μJ/310 μJ, 620 mW at 4.06 μm	31
AGS-I, 45 deg	10	1064 nm, 12.5 ps, 1 μs, 100 MHz/25 Hz	4 to 9	6.8 μJ/680 μJ, 17 mW at 5 μm	32
CSP-I, 90 deg	12.1	1064 nm, 8.6 ps, 1 μs, 450 MHz/20 Hz	6.091 to 6.577, NCPM, TT	3.3 μJ/1.5 mJ, 30 mW at 6.275 μm	33
CSP-I, 90 deg	9.5	1064 nm, 15 to 20 ps, 2 μs, 100 MHz/25 Hz	6.4 to 6.45, NCPM, TT	2.8 μJ/560 μJ, 14 mW at 6.4 μm	34
CSP-I, 90 deg	9.5	1064 nm, 15 to 20 ps, 2 μs, 100 MHz/25 Hz	6.5 to 7	5.5 μJ/1.1 mJ, 27.5 mW at 6.5 μm	35
AGS-I, 49 deg	10		2.9 to 7.1	1.2 μJ/240 μJ, 6 mW at 6.5 μm	
AGS-II, 47 deg	10		4.4 to 8.6	2.6 μJ/520 μJ, 13 mW at 6.5 μm	

Note: TT, temperature tuning, NCPM, noncritical phase-matching. T_P and T_T denote the duration of the micro- and macropulses, respectively.

resistivity and growth habit. The optical damage has been characterized in the present study at ~1 μm, for different repetition rates and pulse durations, relevant to OPO and future SPOPO operation.

2 Optical Damage-Limited Performance of HGS OPOs

Let us illustrate in this section the optical damage-limited operation of HGS, in the same two-mirror, singly resonant, double pump pass OPO cavity that we employed for other materials, too. A diode-pumped Q-switched Nd:YAG laser/amplifier system served as a pump, see Fig. 1, with a bandwidth of 30 GHz (1 cm^{-1}) and M^2 factor of ~1.4. The pump beam reached the HGS crystals after reflection at the ZnSe bending mirror (M2) and passing through the output coupler (OC), which is highly transmitting for pump and idler.

The HGS samples used were a 13.4-mm-long one with an aperture of ~10×13.6 mm^2 cut at $\theta = 52.7$ deg and

$\phi = 45$ deg for type-I (oo-e) interaction for the 4-μm range (HGS-1) and a 10.76-mm-long one with an aperture of ~9.5×9.5 mm^2, cut at $\theta = 50.2$ deg and $\phi = 0$ deg for type-II (eo-e) interaction for the 6.3-μm range (HGS-2), in both cases utilizing only the d_{36} component of the nonlinear tensor. Effective nonlinearity is higher for the type-II HGS (Table 1). Both HGS crystals were antireflection (AR)-coated for the resonated signal wavelength, which resulted in low residual reflectivity for the pump as well.

For such singly resonant OPO configurations, obviously, the bhighest idler extraction can be expected with an OC completely reflecting the signal and transmitting the idler. The main reason to use OCs with partial reflectivity for the signal is to avoid crystal damage at high intracavity signal intensity. There were some differences in the OC and in the cavity length in the two cases described below. With HGS-1, a cavity length of 17 mm was employed. The wedged ZnSe OC had a transmission of 29% at the signal wave and 79%
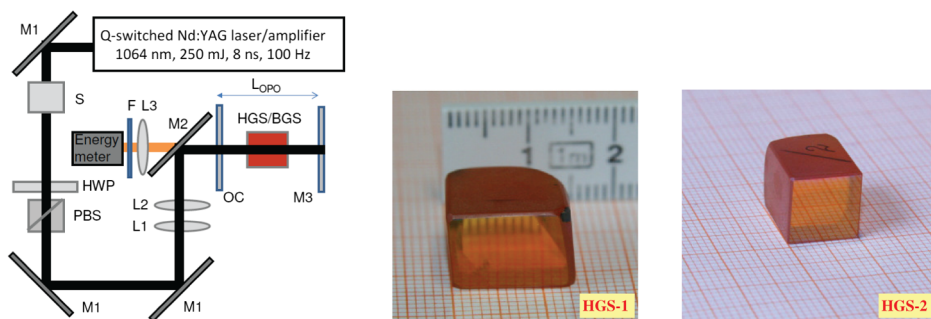

Fig. 1 Optical parametric oscillator (OPO) experimental setup and active elements used: A mechanical shutter (S) can reduce the repetition rate and the average pump power, a half-wave plate (HWP) and a polarizing beam splitter (PBS) are used as attenuator and a telescope consisting of two lenses L1 and L2 expands the pump beam to a diameter of 9.6 and 8.45 mm in the horizontal and vertical directions, respectively. A plane Ag-mirror acts as a total reflector (M3) for all three waves in a double pump pass singly resonant OPO configuration. The filters (F) suppress the residual pump and signal pulses.

for the idler in the case of HGS-1. The ZnS OC used with HGS-2 had radius of curvature of -2 m and transmission of $\sim$30% for the signal wave and 92% for the idler. In this case, the cavity was lengthened to 5.2 cm for better output beam quality. Only the ZnS OC had an AR-coating on its rear surface that enabled improved idler extraction.

The extrapolated threshold with HGS-1 in the 4-μm idler range corresponds to an axial pump fluence of 22 mJ/cm^2 or a peak intensity of $\sim$2.7 MW/cm^2. This is a much lower value than with HGS-2, which can be attributed to the higher parametric gain moving closer to degeneracy, the shorter cavity length, and the longer crystal length. The threshold of $\sim$58 mJ at 6.3 μm with HGS-2 corresponds to an axial pump fluence of 0.18 J/cm^2 or a peak intensity of $\sim$23 MW/cm^2.

Although highest idler energies (of any 1-μm pumped nonoxide OPO) were obtained in case (a) of Fig. 2 and damage-free operation far above threshold ($>$10 times) was possible with this HGS OPO, it is known that highest conversion efficiencies are achieved at lower ratios. The maximum conversion to the idler of $\sim$7.5% is in fact not at maximum pump level but around 40 mJ, which indicates that yet higher output idler energies and average power could be possible if larger apertures of the active element were available. The maximum on-axis intensity applied in this case did not exceed 40 MW/cm^2. Of course, high conversion efficiency means high intracavity signal power, but simultaneously one can expect that the pump is depleted in its maximum.

There is no saturation in the idler energy dependence in case (b) of Fig. 2 due to backconversion, because it was impossible to reach a regime three times above threshold. The maximum pump level in this case was higher, $\sim$55 MW/cm^2 axial intensity, although the conversion efficiency was lower. This was, however, safe for the crystal only at lower (10 Hz) repetition rate. Damage developed immediately at 100 Hz at pump levels above two times threshold, see Sec. 4.

The M^2 factor, measured for the idler, was in the range of 180 to 190 for the two planes in the HGS-1 OPO and improved to $\sim$30 with the longer cavity used in the HGS-2 OPO.

3 Optical Damage of HGS with Focused Beams

In the literature, one finds some systematic optical damage studies on specific NLCs, e.g., ZnGeP$_2$, but no systematic study of such mid-IR NLCs that can be pumped near 1 μm. There exists only one comparative study with 30-ns

long pulses, but it is at a wavelength of 9.55 μm related to CO$_2$ laser frequency doubling.[36] While this study indeed offers the opportunity to compare many NLCs without TPA effect, it is impossible to conclude that the results are useful at 1064 nm. Still it is interesting that HGS showed the highest surface damage resistivity out of nine NLCs in this study ($\sim$300 MW/cm^2 or $\sim$9 J/cm^2 peak axial values), roughly two times higher than AGS. As could be expected, far from the bandgap, different phases of HGS (yellow and orange) or doping with Cd (Cd$_x$Hg$_{1-x}$Ga$_2$S$_4$) gave similar results.

Since often authors do not specify if their damage thresholds correspond to average or peak fluence/intensity, relative measurements are sometimes more informative: thus two times better damage resistivity of HGS compared to AGS was given in Ref. 11. An absolute value of 80 MW/cm^2 (0.3 J/cm^2) for AR-coated HGS was measured at 30 Hz for 5-ns-long pump pulses at 1064 nm for the same sample.[12] For uncoated HGS, measurements with 30-ns pulses outside the OPO indicate damage threshold between 40 and 60 MW/cm^2 (1.2 to 1.8 J/cm^2, basically single shot) at 1064 nm (Ref. 37) and confirm roughly two times better resistivity compared to AGS.[11,36] The surface damage limit we observed in 2-mm thick uncoated yellow HGS with 1-ns 1064-nm pulses at 1 kHz was $\sim$400 MW/cm^2 or $\sim$0.4 J/cm^2 (peak values).[37]

Depending on the excess HgS in the charge, both yellow and orange-phase HGS can be grown.[37] First, we studied four test plates of HGS, which were single-side AR-coated similar to the OPO elements, see Fig. 3. Two of them (HGS-P1 and HGS-P3) were orange-phase and the other two (HGS-P2 and HGS-P4) were yellow phase. The single layer of Al$_2$O$_3$ coating (ELAN Ltd., Saint Petersburg, Russia) was centered at 1280 nm for the signal wavelength but reduced substantially the Fresnel losses also at the pump wavelength of 1064 nm. The aperture of the plates was roughly 10×10 mm^2, the thickness varied from 2.14 to 2.44 mm, and the wedge was between 10 and 30$''$. The cut angle was $\theta \sim 45$ deg, while $\varphi = 0$ deg (HGS-P1) and $\varphi = 45$ deg (HGS-P2 to HGS-P4). We simultaneously tested a yellow color disk sample of CdGa$_2$S$_4$ (CGS-D) with a diameter of 12.5 mm and thickness of 1.6 mm, which was cut at $\varphi = 45$ deg and $\theta = 45$ deg. However, this disk had a different AR-coating on both sides, performed by QTF Inc, Oldsmar, FL. using multilayer structure specified for $<$1% reflection at 1064, 1274, and 6450 nm. Such CGS samples had been tested before with a similar laser source as the one described below but with a pulse duration of 14 ns, and no
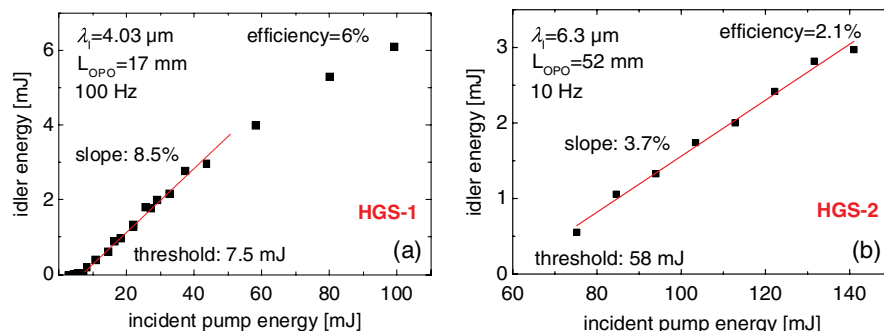

Fig. 2 Input-output OPO characteristics with HGS-1 (a) and HGS-2 (b) with thresholds extrapolated from the idler slope efficiency.

damage was observed up to peak on-axis fluence of 1.6 J/cm^2 using an unfocused beam with a diameter of ~3.8 mm.

The HGS samples are normally single pass saw cut in the crystallographic frame and then polished using alumina particles involving several polishing stages with decreasing grit sizes of 40, 20, 7, 1, and 0.5 μm.

The irradiating source was the same as used for OPO pumping: a diode-pumped Q-switched Nd:YAG laser/amplifier at 1064 nm with a pulse duration of 8 ns operating at 100 Hz. Intensity spatial profile is close to Gaussian distribution and $M^2 \sim 1.4$. The linearly polarized beam passed through plates HGS-P1, HGS-P2, and HGS-P4 as an e-wave and through plate HGS-P3 as an o-wave; its orientation relative to the CGS-D sample was unknown. The beam was focused with a lens with a focal length of 250 mm, and the samples to be tested were placed slightly behind the focus where the area amounted to $S = \pi w^2 = 1.13 \times 10^{-3}$ cm^2, with w denoting the e^{-2} intensity radius. The pulse energy E was varied by a system of a half-wave plate and a polarizer and measured directly in front of the sample with pyroelectric detector. All fluence values given below are peak-on-axial, i.e., $\sim 2 \times E/S$.

Damage threshold of every plate was determined according to a modified (R-on-1) procedure S-on-1, recommended by ISO.[38] Using the R-on-1 method, which defines a 0% probability for damage, as a more rigorous definition of laser damage threshold than the method of simply increasing the incident fluence until damage occurs gives significantly lower values as observed in ZnGeP$_2$ at its OPO pump wavelength.[39] The small spot provided the opportunity to effectively use the test plate surfaces. Fourteen sites on every plate, or seven on each side, were randomly chosen for irradiation. Every site on a given plate was irradiated in a series of exposures, starting from an energy level similar for all sites on a given plate until damage occurred. Thus, damage probability at a given energy level could be calculated as a ratio of number of sites damaged at energies lower or equal to this level to full number of tested sites 14. The obtained distribution of damage probabilities versus energy fluence was then fitted with a linear function, which gave the 0% damage probability for a given plate as the intercept with the energy fluence coordinate axis. Two or three sites on each plate were irradiated before starting the test to estimate expected damage threshold. The exposure time in the tests was 1 min (6000 pulses) and the step between two subsequent exposures was 0.07 J/cm^2 in terms of peak on-axis fluence.

Figure 4 shows the results obtained with HGS-P1 when seven sites were illuminated in each direction. When the AR-coated surface was the front surface, a total of five damages appeared on the rear (uncoated) side and four damages on the front AR-coated side. When the uncoated surface was the front surface, a total of two damages appeared on the front uncoated side and five damages on the rear AR-coated side, although the actual fluence on the rear surface was reduced in this case by the front surface Fresnel reflection. Thus, it cannot be concluded that AR-coating improves the damage resistivity as observed in ZnGeP$_2$ (Ref. 39) because in total seven damage spots on the uncoated side occurred against nine damage spots on the AR-coated side. Although the linear fits in Fig. 4 have different slopes for the two propagation directions, the results can be combined into one plot [Fig. 5(a)] whose linear fit gives a 0%-probability damage threshold of 1.76 J/cm^2. HGS-P2 and HGS-P4 showed lower damage resistivity in both directions compared to HGS-P1, and all damages appeared on the AR-coated side. HGS-P3 had an overall damage threshold higher than HGS-P1, but here all damage craters occurred on the AR-coated side. In the double-side AR-coated CGS-D, most damages occurred on the rear side. The damage threshold was higher [Fig. 5(b)] and the increased slope indicates a more even distribution of surface defects compared with HGS.

It should be noted, however, that in some cases, the fits were not good due to the small number of tested sites as compared to Ref. 39. This is especially true for the lowest values in the second and third columns of Table 4, which summarizes the results. Thus, for the fit giving 0.96 J/cm^2, in fact, no damage was observed below 2.3 J/cm^2, while for the fit giving 1.18 J/cm^2, no damage occurred below 1.5 J/cm^2. Obviously these two cases should be excluded when making conclusions as can be seen from the values of the overall fit in the last table column. Taking an average of these values, the 0%-probability damage threshold for HGS is (1.6 ± 0.2) J/cm^2, which translates into 200 MW/cm^2 and is rather high.

For the above reason, we calculated from the experimental data the average damage thresholds $D_m = \sum D_i n_i/N$, and average error of the mean s from $s^2 = \sum (D_m - D_i)^2 n_i/N(N-1)$, where N is the total number of damaged sites, $N = n_1 + n_2 + \ldots, N = 7$ or 14 in our case. One can define the probability P for the damage threshold D to be, e.g., in the interval $D_m \pm 3s$; then $P(N = 7) = 98\%$ and $P(N = 14) = 99\%$. But one can also fix the probability and leave k as a variable in $D_m \pm ks$. Table 5 shows the results of such a processing of the damage threshold data.

The results in Table 5 can be used to obtain an average value for uncoated HGS. Combining the values when this surface was damaged as front and as rear surface, one obtains $D = (2.52 \pm 0.18)$ J/cm^2, for 94% probability. The damage threshold of AR-coated surface of HGS when this surface is front surface can be obtained by combining the results of the corresponding column in Table 5 as four independent measurements, each of them with equal weight and its own error, which gives $D = (2.44 \pm 0.10)$ J/cm^2, for 94% probability.

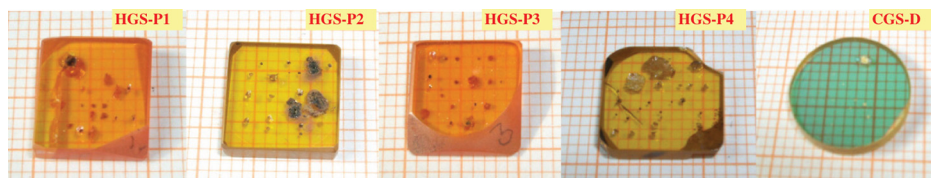**Fig. 3** HgGa$_2$S$_4$ (HGS) damage test plates HGS-P1 to HGS-P4 and CdGa$_2$S$_4$ damage test disk (CGS-D). The small spots are from the damage test described in Sec. 3, while the larger damages are the results of other experiments with larger beam area, see Sec. 4.
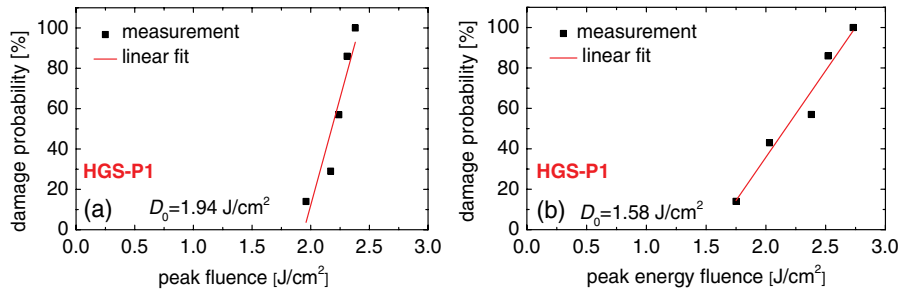
Fig. 4 Damage probability for the single side AR-coated HGS-P1 when the front surface is the AR-coated one (a) and when the front surface is the uncoated one (b). All damages (front and rear surface) are taken into account and the 0%-probability damage threshold D_0 indicated is determined by the intercept of the linear fit with the energy fluence axis.

Similarly, the damage threshold of AR-coated surface when it is rear surface amounts to $D = (2.08 \pm 0.16)$ J/cm^2, for 94% probability.

A different approach is also possible for the results concerning the AR-coated surface of HGS considering all the data on different samples as independent measurements. This (apparently more physical) approach leads to $D = (2.44 \pm 0.11)$ J/cm^2 and $D = (2.07 \pm 0.13)$ J/cm^2, when

the AR-side is front and rear surface, respectively, for 94% probability in both cases. Obviously the two approaches yield almost the same result for the damage threshold of the AR-coated HGS.

In conclusion, damage threshold of HGS under these conditions is very high and seems not to depend on color (phase). AR-coating does not improve it so far, but also does not seriously reduce the surface damage threshold of the front surface. There is definitely dependence on the bandgap, however, because CGS showed higher damage threshold even with multilayer AR-coating. The damage resistivity of uncoated and AR-coated HGS as well as of AR-coated CGS is lower for the rear surface, although the experiments were with a slightly diverging beam, which can be attributed to standing wave effects. In fact, the opposite trend has been described for ZnGeP$_2$,[39,40] but in this case, as already mentioned, the AR-coating improved the ZnGeP$_2$ surface damage resistivity.

4 Optical Damage of HGS with Unfocused Beams Inside and Outside the OPO

Optical damage in HGS occurred at much lower fluence values when such active elements were used in OPOs with large beam sizes (diameters). For the OPO element HGS-1 cut for 4-μm generation, see Fig. 1, bulk damage was observed at ~0.3 J/cm^2 (37.5 MW/cm^2) of peak pump fluence

Table 4 Summary of 0%-probability damage threshold determination in HGS and CGS test plates in terms of peak on-axis fluence.

Damage test sample	AR-coated front surface D_0 (J/cm^2)	Uncoated front surface D_0 (J/cm^2)	Overall D_0 (J/cm^2)
HGS-P1	1.94	1.58	1.76
HGS-P2	1.73	1.18	1.37
HGS-P3	1.88	1.98	1.58
HGS-P4	0.96	1.44	1.68
CGS-D	2.29	—	2.29

Table 5 Summary of the average damage threshold values in terms of peak on-axis fluence and the deviation for 94% probability.

| Damage test sample	AR-coated front surface		Uncoated front surface	
	Damage of front surface, (J/cm^2)	Damage of rear surface, (J/cm^2)	Damage of front surface, (J/cm^2)	Damage of rear surface, (J/cm^2)
HGS-P1	$D_m = 2.29$, $s = 0.03$ $D = (2.29 \pm 0.09)$	$D_m = 2.28$, $s = 0.05$ $D = (2.28 \pm 0.15)$	$D_m = 2.52$	$D_m = 2.05$, $s = 0.13$ $D = (2.05 \pm 0.39)$
HGS-P2	$D_m = 2.38$, $s = 0.08$ $D = (2.38 \pm 0.21)$	$D_m \geq 2.59$	$D_m \geq 2.45$	$D_m = 1.89$, $s = 0.14$ $D = (1.89 \pm 0.32)$
HGS-P3	$D_m = 2.76$, $s = 0.10$ $D = (2.76 \pm 0.26)$	$D_m \geq 3.01$	$D_m \geq 2.45$	$D_m = 2.26$, $s = 0.04$ $D = (2.26 \pm 0.10)$
HGS-P4	$D_m = 2.33$, $s = 0.02$ $D = (2.33 \pm 0.05)$	$D_m \geq 2.45$	$D_m \geq 2.45$	$D_m = 2.11$, $s = 0.08$ $D = (2.11 \pm 0.19)$
CGS-D	—	$D_m = 2.60$, $s = 0.04$ $D = (2.60 \pm 0.09)$	—	—
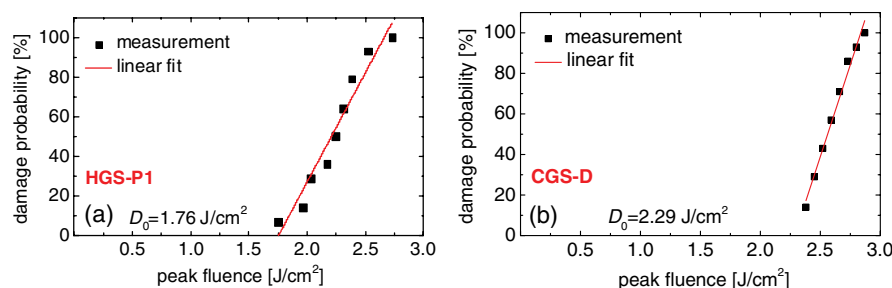
Fig. 5 Average damage probability from illumination in both directions for the single-side AR-coated HGS-P1 (a) and double-side AR-coated CGS-D (b). D_0: 0%-probability damage threshold.

(intensity) after hours of operation when the signal wave was present in the OPO, which corresponds to ~95 mJ in Fig. 2(a), i.e., very close to the maximum pump level applied at 100 Hz. These are incident values and one should bear in mind that there is a double pump pass in this OPO. The damage was a white scattering cloud—one of the rare observations of bulk damage instead of surface damage, see Fig. 6.

While such bulk damage could be hardly observable in the thin plates considered in the previous section, this HGS-1 OPO element was with unknown AR-coating; hence, we focused our attention further on HGS-2, which had the same AR-coating type as the thin damage test plates of HGS described in Sec. 3. We observed formation of similar white clouds inside this type-II HGS crystal when deployed in the double pump pass OPO for idler generation at 6.3 μm. Above 100 mJ of pump energy, they formed quickly (within 30 min) at 100 Hz, and this was the main reason to characterize this OPO at 10 Hz. Figure 7 illustrates the formation of such bulk damage in the HGS-2 OPO element under >100 mJ of pump energy (>0.32 J/cm^2 peak fluence) at 10 Hz. Note that in order to see the cloud, it is necessary to illuminate the crystal with white light. The bulk damage leads to significant reduction of the crystal transmission: with a small (less than the damage size) cw probe beam at 1064 nm, we measured ~10% decrease of the transmission for o-polarization and up to 40% for the e-polarization. With larger beams, the transmission reduction was smeared to <5%. It should be mentioned here that no bulk damage occurred in HGS when the active element was rotated in the cavity by 90 deg so that no oscillation was possible.
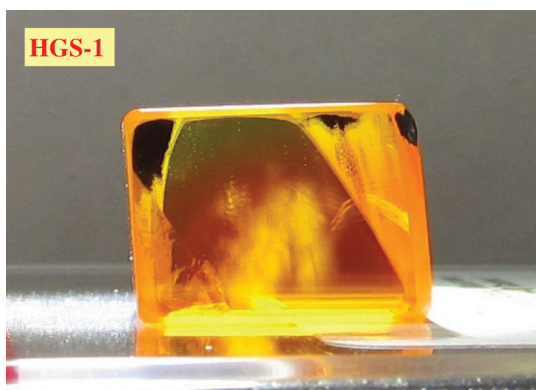

Fig. 6 Bulk damage occurring in the type-I orange-phase HGS-1 OPO element generating 4-μm idler pulses after using it for hours at ~95 mJ pump energy and 100 Hz. The pump beam area is $S = 0.64$ cm^2 in this case.

At maximum pump energy of 140 mJ (on-axis fluence of 0.44 J/cm^2), see Fig. 2(b), eventually first signs of surface damage were seen, though operating at 10 Hz, in the form of dark (burned) spot on the AR-coating, normally on the side toward the closer cavity mirror. For this pump level, we observed intracavity surface damage also when the OPO was not perfectly aligned, generating an idler energy of 1.7 mJ at 10 Hz, compare Fig. 2(b). This is illustrated in Fig. 8. Note that bulk damage in the form of scattering cloud had already occurred beneath the surface spot in the same position and that at the maximum pump fluence we also observed, a few times, damage to the Ag total reflector, Fig. 1.

To verify that this kind of damage is partially related to the signal wave, we immediately proved that no damage occurred to a thick (9.4 mm) sample of $Cd_{0.65}Hg_{0.35}Ga_2S_4$ (CHGS-2, see Fig. 9 left) by irradiating it with 100 mJ of pump energy at 100 Hz outside the cavity. In this case, the beam diameter was reduced to 5 mm (cross-section of $S = 0.2$ cm^2), which corresponds to >1 J/cm^2 peak axial fluence in single pass, but no signs of any damage including bulk clouds were seen after illumination for a reasonable period of 15 min at this higher repetition rate. Since this sample was uncoated, the conclusion basically concerns bulk damage. It is, however, difficult to separate the contribution of signal and pump to the crystal damage occurring when the OPO is operating since the oscillating signal depletes the central part of the pump.

In view of the bulk damage observed in the OPO prior to surface damage, we decided to test available thick samples outside the OPO cavity. These samples shown in Fig. 9 also illustrate the different phases of this nonlinear material.

From left to right on Fig. 9, these were an orange color HGS sample HGS-O cut at $\varphi = 0$ deg, $\theta = 56$ deg, i.e., for type-II phase-matching, with an aperture of 9.23×10 mm^2, length of 10.75 mm, and wedge of ~4 to 5′, whose surface quality was poor; a dark yellow $Cd_{0.27}Hg_{0.73}Ga_2S_4$ (composition in the charge) sample CHGS-1 with an aperture of 13.38×10.08 mm^2 and thickness of 13.62 mm with orientation $\varphi = 45$ deg, $\theta \sim 60$ deg; a 9.4-mm thick yellow $Cd_{0.65}Hg_{0.35}Ga_2S_4$ (composition determined from the short-wave absorption edge with accuracy of ±5 at. % due to unknown orientation and different position of this edge in yellow and orange-phase pure HGS) CHGS-2 with very poor surface polish; and a light yellow color CGS, with an aperture of 12.6×10.5 mm^2, length of 7 mm, and unknown orientation.

These damage tests were performed with the 8-ns 1064-nm pump laser at 100 Hz, choosing a beam cross-section of

Fig. 7 Bulk damage occurring in the type-II orange-phase HGS-2 OPO element generating 6.3-μm idler pulses after using it for hours at >100 mJ pump energy and 10 Hz.
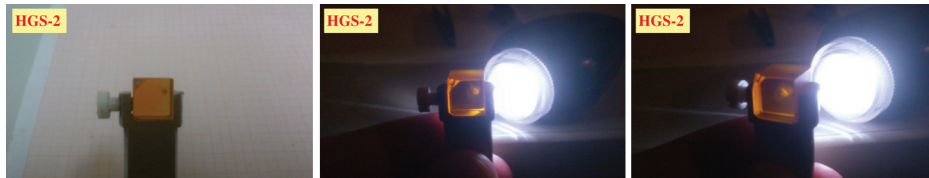

Fig. 8 Surface damage on the HGS-2 OPO element generating 6.3-μm idler pulses at 140 mJ pump energy and 10 Hz.

0.11 cm^2 or diameters of 3.65 and 3.86 mm in the horizontal and vertical directions, respectively, sufficient to cause damage with the available pump energy of 150 mJ. The tests were 10 min long for each step, with an interruption of 2 min between the measurements, starting from 30 mJ and increasing the energy by 10 mJ in each step.

Four tests were performed with each of the uncoated samples and the results are summarized in Table 6. Figure 10 shows crystal shadow patterns obtained by scattered He-Ne laser light, illustrating the damages.

The damage thresholds determined here are systematically lower that the results described in the previous section with focused beams. The main difference is the beam cross-section, which was roughly 100 times smaller in Sec. 3. In particular, comparing uncoated HGS, its damage threshold is about two times higher for small beam sizes. For CGS,

however, this is not necessarily true. One can compare the present results also with the estimation of 2.4 J/cm^2 (peak on-axis) for orange-phase HGS from single shot tests with a beam diameter of 0.4 mm (focused beam with a spot area of 0.0013 cm^2) using 30-ns pulses at 1064 nm (Ref. 41), and this supports the above conclusion.

Surface damage occurs mostly on the rear surface, therefore, front surface damages are exceptions and no changes in the bulk were observed, such as white clouds. However, just before the breakdown, white light is seen in the bulk. Sometimes, such a flash of light is also seen at energies close to the damage limit. In CGS, when the rear surface is damaged, it is not simply a black spot from the breakdown but also a crack (see Fig. 11).

Since no bulk damage was observed in these experiments, we also conducted few longer (60 min) tests at fluence levels below the corresponding surface damage threshold, with all other conditions unchanged. At 41.5 mJ incident energy corresponding to peak on-axis fluence of 0.755 J/cm^2, no signs of damage were seen in HGS-O and the HGS-2 AR-coated OPO element from Figs. 1, 7, and 8. In CHGS-1, no damage was seen at 50 mJ or 0.91 J/cm^2, while in CGS no damage occurred at 82.5 mJ or 1.5 J/cm^2. The only bulk damage observation in the form of clouds was with HGS-O at 45 mJ or 0.82 J/cm^2. This single observation is still evidence that bulk damage can occur solely due to the 1064-nm pump light.

Since the OPOs are pumped in double pass, we tested some of the thick samples also in double pass using an Ag retroreflector for 10-min long exposure tests: surface damage occurred at lower incident fluence, at 0.73 J/cm^2 (40 mJ) in HGS-O (front side) and at 0.76 J/cm^2 (42 mJ)

Table 6 Summary of the average damage threshold values in terms of peak on-axis fluence and the deviation for 94% probability.

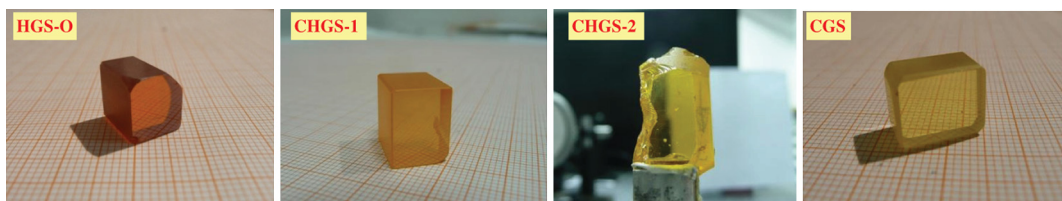| Damage test sample	Average damage threshold (J/cm^2)	Damage on surface
HGS-O	$D = (1.09 \pm 0.22)$	Rear (3), front (1)
CHGS-1	$D = (1.23 \pm 0.26)$	Rear (4)
CHGS-2	$D = (1.50 \pm 0.28)$	Rear (2), front (1), both (1)
CGS	$D = (2.18 \pm 0.22)$	Rear (4)

Fig. 9 Thick damage test elements HGS-O, CHGS-1, CHGS-2, and CGS (from left to right) as described in the text.
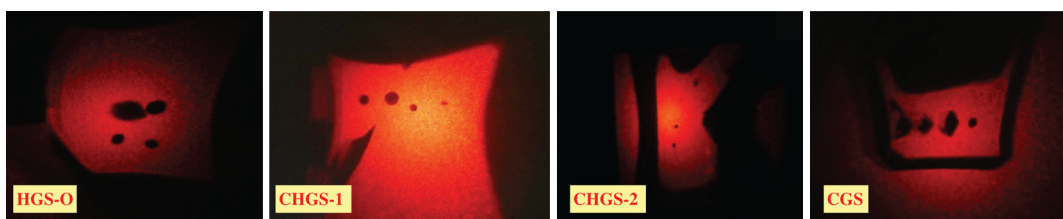
Fig. 10 Crystal shadow patterns for HGS-O, CHGS-1, CHGS-2, and CGS (from left to right), each with four damage spots.

for CHGS-1 (rear side), but no bulk damage was observed. On decreasing the incident fluence to 0.45 J/cm² (25 mJ) in longer (60 min) tests, no bulk damage in the form of clouds occurred in HGS-O and the AR-coated orange-phase HGS-2 OPO element. The latter is a clear indication that bulk damage has lower threshold in the presence of the signal wave when the HGS crystal is inside the operating OPO. Concerning surface damage, the threshold values (fluence) are ~50% higher than inside the OPO. Having in mind that surface damage occurs apparently independent of the repetition rate and the fact that we compare uncoated orange HGS in the extracavity test with AR-coated HGS in the OPO, the difference seems not so dramatic, i.e., the increase of the surface damage probability inside the OPO cavity is much less pronounced than the susceptibility to bulk damage formation.

Finally, in Fig. 12, we illustrate the process of surface damage formation with large (unfocused) beams in HGS. The sample is the orange-phase HGS-P3 shown in Fig. 3 where such damages can be seen as large spots. Figure 12 consists of snapshots from a video recorded at an incident energy of ~45mJ at 100 Hz. For a pump spot of 3.65× 3.86 mm² (diameters), this corresponds roughly to 0.8 J/cm², which is above the damage threshold of the AR-coated front surface.

5 cw and Quasi-cw Damage Studies

Damage tests with cw laser sources are useful in order to rule out effects from the average power in nanosecond OPOs like macroscopic heating. We studied some of the thick uncoated samples described in the previous section with a true cw laser at 1064 nm that had an elliptic beam cross-section with Gaussian diameters of 1.78 and 1.57 mm in the horizontal and vertical planes, respectively, or an area of 0.022 cm²

Fig. 11 Rear surface crack observed in CGS.

in the position of the crystal tested. Crystals CHGS-2 and HGS-O were tested for exposition of 7 min and no damage of any kind occurred up to 5.5 W of incident power, which corresponds to a peak on-axis cw intensity of >500 W/cm². This is more than an order of magnitude higher than the maximum values in the 100 Hz HGS OPO [Fig. 2(a)], having in mind that the beam cross-section is 29 times smaller in the cw case, while the maximum average power applied in the OPO was 10 W. It is also five times higher than in the extracavity damage test of CHGS-2 (100 mJ, 8-ns pulses at 100 Hz) described in the previous section, which also produced no damage.

The following damage test experiments were performed with the objective to evaluate potential application of HGS in a steady-state picosecond or femtosecond SPOPO. The pump sources were Yb-fiber lasers. The picosecond version operated at 80 MHz and produced 5.5-ps long pulses at 1032 nm. The femtosecond version operated at 53 MHz, generating pulses of 220-fs duration at 1035 nm. Both lasers were, however, not bandwidth limited and the Fourier transform of the spectrum corresponded to ~2 ps and ~100 fs, respectively. The tested samples were the ~2 − mm thick plates described in Sec. 3 and shown in Fig. 3. With an $f = 10$ cm lens, the spot size achieved with the picosecond Yb-laser was 90×100 μm² (diameters), which corresponds to $S = 7.1 \times 10^{-5}$ cm². The beam cross-section with the femtosecond Yb-laser achieved with an $f = 20$ cm lens was similar, with Gaussian diameters of 91 and 94 μm corresponding to $S = 6.7 \times 10^{-5}$ cm². The tests were performed for 1 to 30 min, but the results were independent of this illumination time and when damage occurred, this happened within a few seconds. Three different sites were tested for with each sample in each direction of propagation with a separation of roughly 1 mm in order to avoid the effect of previous damage. The results were, however, quite reproducible (better than 5%), and the values in Table 7 correspond to the minimum incident power for which damage was observed.

Nonphase-matched second-harmonic generation (SHG) was the best indicator of laser damage. It was visible both with picosecond and femtosecond pulses; its shape changed when thermal effects set on, and finally it disappeared when damage occurred. In the case of the picosecond laser source, the maximum incident quasi-cw (or average) power was 9.3 W, and damage threshold could not be reached with the double-side AR-coated CGS-D disk and the orange-phase HGS-P1 and HGS-P3 plates when the uncoated side was front surface. Thus, damage threshold was always higher for the uncoated surface of HGS, but the difference did not exceed 10%, see Table 7. The threshold for the occurrence of thermal effects was between 5 and 7 W of incident power and correlated with the damage threshold values for the different HGS samples, which corresponded to 7.3 to
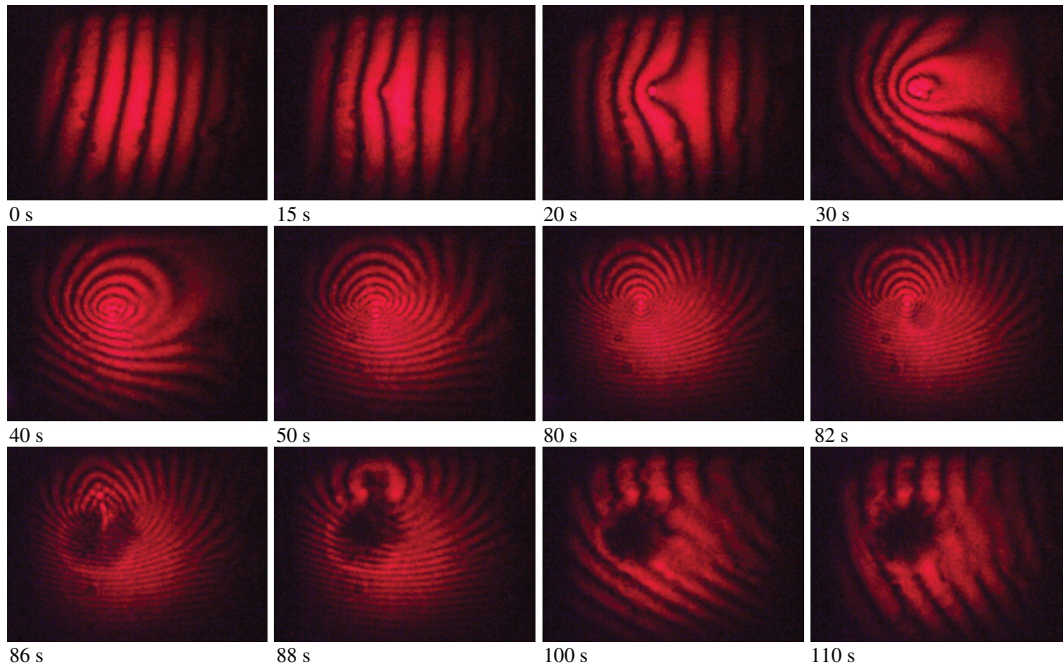
Fig. 12 Damage of the front AR-coated surface of orange HGS recorded at 0.8 J/cm^2 fluence at 1064 nm and 100 Hz. Irradiation starts from the 10th second and heating centered in the beam is modifying the interference pattern; small damage occurs at 82 s, however, off the center, and full damage at 88 s. At 90 s, the irradiation is stopped and the interference fringes start moving backward.

9.1 W. No thermal effects were observed in CGS at all. Damage in HGS was in most cases bulk damage, which started from the front surface but developed through the entire thickness. There were some exceptions only with HGS-P1 when rear uncoated surface damage was seen, which can again be attributed to secondary (standing wave) effects.

The maximum incident quasi-cw power of the femtosecond Yb-fiber laser was 4.8 W, sufficient to reach the damage threshold for all samples except CGS-D (Table 7). In most cases, surface damage on both sides was observed; in a few cases, the damage extended through the whole crystal, and more as an exception, only one surface showed damage. The uncoated surface had again a slightly higher damage threshold, but the difference was even less pronounced. However, the relative damage resistivity of the four HGS test plates was similar to the picosecond regime and the orange phase was again more resistant to damage. Comparing the values for the

Table 7 Summary of the damage threshold values obtained with quasi-cw laser sources.

Damage test sample	Picosecond Yb-laser, 80 MHz/5.5 ps		Femtosecond Yb-laser, 53 MHz/220 fs	
	AR-coated front surface	Uncoated front surface	AR-coated front surface	Uncoated front surface
HGS-P1	$I_{qcw} = 257$ kW/cm^2 $I_p = 585$ MW/cm^2 $D = 3.22$ mJ/cm^2	$I_{qcw} > 263$ kW/cm^2 $I_p > 598$ MW/cm^2 $D > 3.29$ mJ/cm^2	$I_{qcw} = 98.2$ kW/cm^2 $I_p = 8.43$ GW/cm^2 $D = 1.85$ mJ/cm^2	$I_{qcw} = 95.3$ kW/cm^2 $I_p = 8.17$ GW/cm^2 $D = 1.80$ mJ/cm^2
HGS-P2	$I_{qcw} = 178$ kW/cm^2 $I_p = 405$ MW/cm^2 $D = 2.23$ mJ/cm^2	$I_{qcw} = 190$ kW/cm^2 $I_p = 431$ MW/cm^2 $D = 2.37$ mJ/cm^2	$I_{qcw} = 65.5$ kW/cm^2 $I_p = 5.62$ GW/cm^2 $D = 1.24$ mJ/cm^2	$I_{qcw} = 71.4$ kW/cm^2 $I_p = 6.13$ GW/cm^2 $D = 1.35$ mJ/cm^2
HGS-P3	$I_{qcw} = 243$ kW/cm^2 $I_p = 553$ MW/cm^2 $D = 3.04$ mJ/cm^2	$I_{qcw} > 263$ kW/cm^2 $I_p > 598$ MW/cm^2 $D > 3.29$ mJ/cm^2	$I_{qcw} = 86.3$ kW/cm^2 $I_p = 7.40$ GW/cm^2 $D = 1.63$ mJ/cm^2	$I_{qcw} = 101$ kW/cm^2 $I_p = 8.68$ GW/cm^2 $D = 1.91$ mJ/cm^2
HGS-P4	$I_{qcw} = 198$ kW/cm^2 $I_p = 450$ MW/cm^2 $D = 2.48$ mJ/cm^2	$I_{qcw} = 215$ kW/cm^2 $I_p = 489$ MW/cm^2 $D = 2.69$ mJ/cm^2	$I_{qcw} = 68.5$ kW/cm^2 $I_p = 5.87$ GW/cm^2 $D = 1.29$ mJ/cm^2	$I_{qcw} = 74.4$ kW/cm^2 $I_p = 6.38$ GW/cm^2 $D = 1.40$ mJ/cm^2
CGS-D	$I_{qcw} > 263$ kW/cm^2 $I_p > 598$ MW/cm^2 $D > 3.29$ mJ/cm^2	—	$I_{qcw} > 143$ kW/cm^2 $I_p > 12.3$ GW/cm^2 $D > 2.70$ mJ/cm^2	—

Note: I_{qcw} is the peak on-axis quasi-cw intensity, I_p is the peak on-axis pulse intensity, and D is the peak on-axis pulse fluence.

quasi-cw and pulse intensities as well as the pulse fluence in the picosecond and femtosecond regimes (Table 7) indicates that none of these parameters alone defines the damage behavior, but the dependence both on the average power and the pulse duration shall be considered. Also, in the femtosecond regime, the threshold for the occurrence of thermal effects correlated with the damage threshold of the different samples; in terms of incident average power, the former varied from 1.5 to 3 W and the latter from 2.2 to 3.4 W. The different threshold for the onset of thermal effects confirms that higher-order nonlinear processes cannot be ruled out in the femtosecond regime and both TPA and self-focusing might affect the damage behavior in this case.

If the primary goal of the singly resonant SPOPO is conversion to the mid-IR in the idler wave, then the signal need not be out-coupled and the idler will be generated by difference-frequency mixing in a single pass. In this case, the fixed-field approximation can be used and Table 8 gives the acceptance angle (FWHM) and the group-velocity mismatch (GVM) parameters calculated assuming plane waves. Temporal/spatial walk-off of the idler will then affect only its pulse duration but not the conversion efficiency, which will be primarily determined by the Δ_{32} GVM parameter. It is clear then that type-II (eo-e) phase-matching is advantageous in all parameters, the most important of which is the 38% higher effective nonlinearity. Taking into account the spectral extension of the laser outputs for the picosecond pump laser, the HGS crystal could then be as long as 36 mm, while for the femtosecond version, the limit is ~2 mm. The Rayleigh range obtained with the picosecond pump laser amounted to 11.6 mm (inside the crystal) and the divergence (full angle) was 42 mrad. For the femtosecond Yb-fiber laser, these parameters were 15.8 mm and 28 mrad. Thus, the Rayleigh ranges still permit crystals as long as 10 to 15 mm to be used, but the spatial walk-off and angular acceptance represent the most severe limitations. Thus, it is questionable if the parametric gain will be sufficient in the picosecond regime. To utilize safely the full available power of the femtosecond Yb-fiber laser and avoid both damage and thermal effects, it seems necessary to use an

Table 8 Summary of essential crystal parameters for SPOPO operation of HGS pumped at 1030 nm with idler generation at 6450 nm. The angular acceptance corresponds to FWHM of the conversion efficiency in the low signal limit and the group-velocity dispersion (GVM) parameters $\Delta_{ij} = 1/v_i - 1/v_j$ are defined as differences of the corresponding inverse group velocities.

Parameter	Type-I (oo-e) HGS	Type-II (eo-e) HGS
Phase-matching angle θ (deg)	45.4	50.6
Effective nonlinearity d_{eff} (pm/V)	17.5	24.1
Refractive index n (1030 nm)	2.46186	2.45782
Spatial walk-off $\tan \rho_3 / \tan \rho_1$	0.0182/—	0.0178/0.0171
GVM $\Delta_{31}/\Delta_{32}/\Delta_{21}$ (fs/mm)	325/71.6/254	390/55.3/334
Angular acceptance $\Delta\theta \times L$ (mrad × mm)	20.4	24.6

$f = 40$ cm lens and reduce the focused pump intensity by a factor of 4. A twice reduced pump beam divergence is then compatible with a crystal thickness of ~2 mm, which will have adequate angular acceptance. The spatial walk-off will then be roughly five times smaller than the pump beam diameter. This scenario seems quite realistic since the damage threshold and the thermal effects were estimated in this section for a similar HGS thickness of ~2 mm. The parametric gain [exponential field gain factor defined from $I_s(L) = 1/4 I_s(0) \exp(2\Gamma L)$), where I_s denotes the signal intensity], assuming plane waves and neglecting the spatial and temporal walk-off effects, amounts to $\Gamma \sim 12$ cm^{-1} for a pump intensity of 1 GW/cm^2 in type-II HGS or $\Gamma L \sim 2.4$ for $L = 2$ mm, which gives small signal intensity amplification of ~30. Such gain is very close to the one of a 2-mm periodically poled LiNbO$_3$ crystal (the most widely used oxide material in steady-state SPOPOs pumped near 1 μm) tuned to a typical idler wavelength of ~4 μm.

6 Conclusion

While HGS is probably the best nonlinear crystal for 1-μm pumped mid-IR downconversion, its performance in nanosecond OPOs is severely limited by optical damage. Surface damage in extracavity experiments measured on this time scale depends on the beam size and occurs at lower fluence at 1064 nm for larger beam sizes, which is related to the probability of finding a surface defect within the illuminated spot. Existing AR-coatings seem not to enhance the surface damage resistivity of HGS and there is obviously room for improvement. However, at present, this turns out to be a secondary problem because bulk damage in the form of scattering centers (white clouds) occurs at lower pump levels at 1064 nm. We cannot rule out that surface damage is a consequence of bulk and undersurface damage in the cases when such occur. The observation of lower bulk damage threshold contradicts the widely spread opinion that surface damage of such nonlinear crystals is the main limitation. Bulk damage can be observed when irradiating the crystal only by nanosecond pump pulses at 1064 nm; however, such damage occurs at substantially lower levels when the crystal is deployed in the OPO and the circulating signal power is sufficiently high. The minimum pump fluence for which we observed strong formation of such defects in a double pass pumped HGS OPO at 100 Hz was 0.3 J/cm^2, but the threshold should be even lower because the detection limit depends on the illumination time. Thus, reduction of the repetition rate does not solve the problem and there is no cumulative damage; only the process of defect formation is slowed down. Surface damage in the OPO also occurs at lower pump levels than extracavity, but this is still at least 50% above the bulk damage threshold of orange-phase HGS. Nevertheless, comparison of single-pass and double-pass damage tests with intracavity surface damage observations, in particular when the OPO is misaligned, indicates reasonable correspondence and hence no essential contribution of the other two waves (signal or idler) to the surface damage formation.

The existence of different phases (stoichiometry) of HGS additionally complicates the study of light-induced optical damage. With focused beams, when the surface damage threshold is >2 J/cm, no significant difference between the phases is evident. Cd-doped HGS exhibits higher surface

damage threshold in the nanosecond regime, at least for large beam sizes. We never observed bulk damage in the form of clouds in CHGS, but unfortunately no AR-coated samples of this kind were available for intracavity OPO tests. Pure CGS exhibited the highest damage resistivity and this also seems related to lowest concentration of defects. The surface damage resistivity of CGS seems not deteriorated by AR-coating and can serve as an orientation for the maximum achievable damage resistivity of HGS, which should be >2 J/cm in terms of peak on-axis fluence.

We associate the lower damage resistivity of HGS when used in the OPO with the signal wave because it is resonated and is much closer to the bandgap, but there is no direct evidence that it is the signal and not the idler wave. (Note that resonating the idler as suggested in early OPO literature is not a solution because such dielectric mirrors themselves have low damage resistivity.) In any case, the damage effect is not related to a resonance because we observed bulk damage formation at different signal wavelengths (OPOs generating 4.03 and 6.3 μm idler output, Fig. 2). In fact, for the OPO elements studied here, the residual absorption at the signal wave was very low, typically <2%/cm, while the idler absorption at 6.3 μm was typically 10%/cm or even more. We have no explanation for the large residual mid-IR absorption of the present HGS samples and this will be studied in the near future. In any case, comparative transmission measurements of thick samples in the mid-IR indicate that orange-phase HGS exhibits reduced transmission compared to yellow phase HGS or CGS. Moreover, the transmission of orange HGS decreases significantly starting from ~4 μm, while that of yellow HGS and CGS does not change up to ~9 μm. We performed some preliminary extracavity damage tests using the idler OPO output at 6.3 μm and 10 Hz repetition rate, but the achievable focused fluence was limited. In any case, no visible damage was detected in the HGS-O test element up to a peak fluence of 0.6 J/cm^2 in the focal spot of 0.22 mm diameter (area of 4×10^{-4} cm^2) in two runs of 10 min each, which is evidence that at least the idler alone is not the main damage factor inside the OPO.

In support of the role of the signal wave, it should be outlined that the signal pulses in such OPOs make many round-trips and experience multiple absorption losses. Thus, a great part of their energy is absorbed in the nonlinear crystal. Increasing the output coupling has been often considered in the literature as a solution to reduce the intracavity signal power, but for the present singly resonant OPOs, the oscillation threshold is already too high to afford increased signal losses. In the extreme limit of no output coupler, highly nonlinear crystals as HGS could operate as optical parametric generators or OPOs with low finesse cavity due to idler reflectivity of the crystal faces.[42] Indeed, removing the output coupler from the setup in Fig. 1, with the HGS-2 crystal for 6.3 μm generation, we observed such operation with a slightly higher threshold but lower slope efficiency, which resulted in maximum conversion efficiency of 1.4% from pump to idler [compare with Fig. 2(b)] or 2.06 mJ of idler energy at 147 mJ incident pump energy. No bulk damage was observed in this experiment, which means that conversion efficiency could be possibly improved by using tighter focusing in comparison to the OPO case. Note that this setup is also equivalent to the use of HGS as optical parametric amplifier (OPA) because the scheme

is double pass and the beam cross-section can be varied in the two passes.

From a practical point of view, the information extracted from extracavity nanosecond measurements seems of limited value because it is difficult to simulate the situation in the OPO in the presence of more waves. Testing of passive (non-phase-matched) elements in the OPO cavity is not expected to provide more information than inspecting the OPO element itself. Thus, our primary interest in the future will be manufacturing of yellow phase and/or Cd-doped HGS active elements for the OPO. This is absolutely important for the HGS crystal because the present situation indicates very low damage resistivity (comparable to many other chalcogenide mid-IR crystals applicable for 1-μm pumping) and similar to CSP, energy scaling is limited notwithstanding the high FM of HGS. Finally, since the isostructural CGS crystal (unfortunately lacking sufficient birefringence), which can be grown colorless, showed much better reproducibility in the damage tests, bulk damage was never observed, and the results were rather insensitive to the surface quality or the presence or absence of AR-coating; we conclude that these properties are possibly related to a lower concentration of defects, leading to weaker dependence of the damage threshold on the beam size.

It is difficult to predict if it will be possible in the future to understand the defect formation mechanisms in HGS and find an appropriate solution. In any case, when OPO operation is limited by crystal damage, one has to search for alternative strategies to avoid it. Some of them are known, e.g., using top-hat pump beam profiles to avoid the on-axis peak of the intensity. Other approaches for homogenization of the spatial beam profile and phase, like the rotated image singly resonant twisted rectangle concept, have proven very effective in mid-IR OPOs pumped in the 2-μm range.[43] The fluence dependence of the damage threshold also indicates that using shorter pump pulses (e.g., 1 ns) is another alternative.[24] Pulses of 1 ns duration could be advantageous also for adding an OPA stage with sufficient gain, i.e., relaxing the energy requirements to the OPO and boosting the output in a subsequent OPA stage, but this will require the development of novel, nonstandard laser pump systems.[44]

SPOPOs offer another possibility to obtain high-average powers in the mid-IR, but operation in the steady-state with 1-μm pumping has not been demonstrated with a nonoxide NLC, yet. We evaluated the potential of HGS for such a regime using novel high-repetition rate (50 to 100 MHz) picosecond and femtosecond pump sources. Due to additional restrictions related to the tight focusing, shorter samples in combination with femtosecond pump pulse durations seem more promising. Damage formation, studied near 1030 nm, is a complex phenomenon then, with surface and bulk effects and dependence both on the quasi-cw and pulse peak intensities. These limitations have to be taken into account when designing the pump geometry, and our evaluations show that HGS samples cut for type-II phase matching with a thickness of ~2 mm are optimum for 100- to 200-fs pump pulse durations. We have no explanation why at such extremely tight focusing the orange phase (the one with the smaller bandgap) showed better thermal resistivity both with picosecond and with femtosecond pulses at high repetition rates.

References

1. E. O. Amman and J. M. Yarborough, "Optical parametric oscillation in proustite," *Appl. Phys. Lett.* **17**(6), 233–235 (1970).
2. D. C. Hanna et al., "Reliable operation of a proustite parametric oscillator," *Appl. Phys. Lett.* **20**(1), 34–36 (1972).
3. D. C. Hanna, B. Luther-Davies, and R. C. Smith, "Singly resonant proustite parametric oscillator tuned from 1.22 to 8.5 μm," *Appl. Phys. Lett.* **22**(9), 440–442 (1973).
4. Y. X. Fan et al., "AgGaS$_2$ infrared parametric oscillator," *Appl. Phys. Lett.* **45**(4), 313–315 (1984).
5. P. B. Phua et al., "Nanosecond AgGaS$_2$ optical parametric oscillator with more than 4 micron output," *Jpn. J. Appl. Phys.* **36**(12B), L1661–L1664 (1997).
6. T. H. Allik et al., "Advances in optical parametric oscillators with application to remote chemical sensing," *Proc. SPIE* **3383**, 58–64 (1998).
7. K. L. Vodopyanov et al., "AgGaS$_2$ optical parametric oscillator continuously tunable from 3.9 to 11.3 μm," *Appl. Phys. Lett.* **75**(9), 1204–1206 (1999).
8. T.-J. Wang et al., "Wide-tunable, high energy AgGaS$_2$ optical parametric oscillator," *Opt. Express* **14**(26), 13001–13006 (2006).
9. T.-J. Wang et al., "Model and experimental investigation of frequency conversion in AgGaGe$_x$S$_{2(1+x)}$ ($x = 0, 1$) crystals," *J. Phys. D: Appl. Phys.* **40**(5), 1357–1362 (2007).
10. T. J. Wang et al., "3-5 μm AgGaS$_2$ optical parametric oscillator with prism cavity," *Laser Phys.* **19**(3), 377–380 (2009).
11. E. Takaoka and K. Kato, "Tunable IR generation in HgGa$_2$S$_4$," presented at *Conf. on Lasers and Electro-Optics*, paper CWF39, OSA, San Francisco, California (3–8 May 1998).
12. K. Kato and K. Miyata, "Nd:YAG laser pumped HgGa$_2$S$_4$ parametric oscillator," *Proc. SPIE* **8604**, 86041K (2013).
13. V. V. Badikov et al., "A HgGa$_2$S$_4$ optical parametric oscillator," *Quantum Electron.* **33**(9), 831–832 (2003).
14. V. V. Badikov et al., "Optical parametric mid-IR HgGa$_2$S$_4$ oscillator pumped by a repetitively pulsed Nd:YAG laser," *Quantum Electron.* **37**(4), 363–365 (2007).
15. A. Tyazhev et al., "High-power HgGa$_2$S$_4$ optical parametric oscillator pumped at 1064 nm and operating at 100 Hz," *Laser Photonic Rev.* **7**(4), L21–L24 (2013).
16. J. Mangin et al., "Comprehensive formulation of temperature-dependent dispersion of optical materials: illustration with case of temperature tuning of a mid-IR HgGa$_2$S$_4$ OPO," *J. Opt. Soc. Am. B* **26**(9), 1702–1709 (2009).
17. A. Esteban-Martin et al., "High-energy optical parametric oscillator for the 6 μm spectral range based on HgGa$_2$S$_4$ pumped at 1064 nm," *Laser Photonics Rev.* **7**(6), L89–L92 (2013).
18. V. V. Badikov et al., "Optical parametric oscillator on an Hg$_{1-x}$Cd$_x$Ga$_2$S$_4$ crystal," *Quantum Electron.* **35**(9), 853–856 (2005).
19. J.-J. Zondy et al., "LiInSe$_2$ nanosecond optical parametric oscillator," *Opt. Lett.* **30**(18), 2460–2462 (2005).
20. G. Marchev et al., "Nd:YAG pumped nanosecond optical parametric oscillator based on LiInSe$_2$ with tunability extending from 4.7 to 8.7 μm," *Opt. Express* **17**(16), 13441–13446 (2009).
21. G. Marchev et al., "Broadly tunable LiInSe$_2$ optical parametric oscillator pumped by a Nd:YAG laser," *Proc. SPIE* **7487**, 74870F (2009).
22. A. Tyazhev et al., "LiInSe$_2$ nanosecond optical parametric oscillator tunable from 4.7 to 8.7 μm," *Proc. SPIE* **7582**, 75820E (2010).
23. V. Petrov et al., "Non-critical singly resonant OPO operation near 6.2 μm based on a CdSiP$_2$ crystal pumped at 1064 nm," *Opt. Lett.* **34**(16), 2399–2401 (2009).
24. V. Petrov et al., "Subnanosecond, 1 kHz, temperature-tuned, noncritical mid-infrared optical parametric oscillator based on CdSiP$_2$ crystal pumped at 1064 nm," *Opt. Lett.* **35**(8), 1230–1232 (2010).
25. G. Marchev et al., "1064 nm pumped CdSiP$_2$ optical parametric oscillator generating sub-300 ps pulses near 6.15 μm at 1-10 kHz repetition rates," *Opt. Commun.* **291**, 326–328 (2013).
26. G. Marchev et al., "Comparison of linear and RISTRA cavities for a 1064 nm pumped CdSiP$_2$ OPO," *Proc. SPIE* **8240**, 82400E (2012).
27. A. Tyazhev et al., "Singly-resonant optical parametric oscillation based on the wide band-gap mid-IR nonlinear optical crystal LiGaS$_2$," *Opt. Mater.* **35**(8), 1612–1615 (2013).
28. A. Tyazhev et al., "Midinfrared optical parametric oscillator based on the wide-bandgap BaGa$_4$S$_7$ nonlinear crystal," *Opt. Lett.* **37**(19), 4146–4148 (2012).
29. A. G. Jackson, M. C. Ohmer, and S. R. LeClair, "Relationship of the second order nonlinear optical coefficient to energy gap in inorganic non-centrosymmetric crystals," *Infrared Phys. Technol.* **38**(4), 233–244 (1997).
30. E. C. Cheung, K. Koch, and G. T. Moore, "Silver thiogallate, singly resonant optical parametric oscillator pumped by a continuous-wave mode-locked Nd:YAG laser," *Opt. Lett.* **19**(9), 631–633 (1994).
31. K. J. McEwan, "High-power synchronously pumped AgGaS$_2$ optical parametric oscillator," *Opt. Lett.* **23**(9), 667–669 (1998).
32. A. A. Mani et al., "Pumping picosecond optical parametric oscillators by a pulsed Nd:YAG laser mode locked using a nonlinear mirror," *Appl. Phys. Lett.* **79**(13), 1945–1947 (2001).
33. S. C. Kumar et al., "Compact, 1.5 mJ, 450 MHz, CdSiP$_2$ picosecond optical parametric oscillator near 6.3 μm," *Opt. Lett.* **36**(16), 3236–3238 (2011).
34. A. Peremans et al., "Noncritical singly resonant synchronously pumped OPO for generation of picosecond pulses in the mid-infrared near 6.4 μm," *Opt. Lett.* **34**(20), 3053–3055 (2009).
35. N. Hendaoui et al., "Synchronously pumped OPO for picosecond pulse generation in the mid-infrared near 6.45 μm using AgGaS$_2$ and CdSiP$_2$: a comparative study," *Laser Phys.* **23**(8), 085401 (2013).
36. Yu. M. Andreev et al., "Radiation resistance of nonlinear crystals at a wavelength of 9.55 μm," *Quantum Electron.* **31**(12), 1075–1078 (2001).
37. V. Petrov, V. Badikov, and V. Panyutin, "Quaternary nonlinear optical crystals for the mid-infrared spectral range from 5 to 12 micron," in *Mid-Infrared Coherent Sources and Applications*, M. Ebrahim-Zadeh and I. Sorokina, Eds., pp. 105–147, Springer, Dordrecht, The Netherlands (2008).
38. ISO standard, ISO 11254-2, Lasers and laser-related equipment—Determination of laser-induced damage threshold of optical surfaces—Part 1: 1-on-1 test, and Part 2: S-on-1 test (2001).
39. K. T. Zawilski et al., "Increasing the laser-induced damage threshold of single-crystal ZnGeP$_2$," *J. Opt. Soc. Am. B* **23**(11), 2310–2316 (2006).
40. R. D. Peterson et al., "Damage properties of ZnGeP$_2$ at 2 μm," *J. Opt. Soc. Am. B* **12**(11), 2142–2146 (1995).
41. V. V. Badikov et al., "A study of the optical and thermal properties of nonlinear mercury thiogallate crystals," *Quantum Electron.* **34**(5), 451–456 (2004).
42. G. Marchev et al., "Optical parametric generation in CdSiP$_2$ at 6.125 μm pumped by 8 ns long pulses at 1064 nm," *Opt. Lett.* **37**(4), 740–742 (2012).
43. G. Stoeppler, M. Schellhorn, and M. Eichhorn, "Enhanced beam quality for medical applications at 6.45 μm by using a RISTRA ZGP OPO," *Laser Phys.* **22**(6), 1095–1098 (2012).
44. D. Chuchumishev et al., "Single-frequency MOPA system with near-diffraction-limited beam quality," *Quantum Electron.* **42**(6), 528–530 (2012).

Biographies and photographs of the authors not available.